

Instability and nonlinear dynamics of the MJO in a tropical channel model with vertically-varying convective adjustment

H. Reed Ogrosky · Samuel N. Stechmann ·
Scott Hottovy

April 17, 2019 - Revised

Received: date / Accepted: date

Abstract In the tropical atmosphere, weather and climate are influenced by dispersive equatorial waves and their coupling with water vapor, deep convection, and rainfall. The dominant mode of variability on intraseasonal time scales is the Madden–Julian Oscillation (MJO), which is still not fully understood. Here we investigate the question: Is the MJO a linearly stable wave or an unstable wave? The linearly stable (i.e. damped) MJO regime, in which case random stochastic forcing provides the source for MJO variability, was previously investigated in a linear version of a model that has a convective adjustment parameterization. Here, to assess the other alternative, nonlinearity is added to the model and allows the study of the linearly unstable MJO regime. Model simulations are performed and evaluated for their ability to generate MJO variability as well as the full spectrum of tropical variability such as convectively coupled equatorial waves (CCEWs). In simulations of unstable growth, nonlinear advection slows the growth, and the wave saturates with reasonable amplitude, structure, speed, and dynamics. In further tests, MJO instability can sometimes excite CCEW variability, but only in a subset of cases. Overall, both the stable and unstable MJOs appear to be reasonable and may arise in different situations due to different environmental conditions.

Keywords Dispersive equatorial waves · Madden-Julian oscillation · Stability analysis · Nonlinear dynamics

H. Reed Ogrosky
Department of Mathematics and Applied Mathematics
Virginia Commonwealth University
Richmond, VA, USA
Tel.: 804-828-0459
E-mail: hrogrosky@vcu.edu

Samuel N. Stechmann
Department of Mathematics, University of Wisconsin-Madison, Madison, WI, USA
Department of Atmospheric and Oceanic Sciences, University of Wisconsin-Madison, Madison, WI, USA

Scott Hottovy
Department of Mathematics, United States Naval Academy, Annapolis, MD, USA

1 Introduction

The fluid dynamics of the tropical atmosphere involves a complex blend of dispersive equatorial waves, moist convection, clouds, and rainfall [6, 12, 21, 23, 30, 54]. The waves and convection are coupled together in ways that are not fully understood. For instance, latent heating results from phase changes of water within clouds, and it can further drive atmospheric circulations; moreover, atmospheric circulations can modulate the occurrence of water vapor and clouds.

The Madden-Julian oscillation (MJO) is the dominant component of tropical variability on intraseasonal timescales, with a timescale of 20-100 days [4, 5, 19, 24, 27–29, 54, 55]. There is much variability from one event to another, but the MJO often moves eastward with a phase speed of roughly $3\text{--}8\text{ m s}^{-1}$, a typical wavelength in the range of 12,000 to 20,000 km [38, 54], and a horizontal structure that resembles components of two types of equatorial waves: equatorial Rossby and Kelvin waves [8, 54]. The MJO plays an important role in global weather and climate, as it has impacts on tropical cyclones [25, 33], El Niño–Southern Oscillation [9], active and break phases of monsoons [24], and midlatitude weather and its predictability [15, 16].

Some fundamental questions about the MJO remain, however, including: Is the MJO linearly stable (i.e. damped), neutral, or unstable? This is the main motivating question of this paper, and is a question about the nature of the MJO itself, and what creates MJO variability. For instance, the MJO could be a linearly unstable mode in which case the background environment provides the energy for the MJO’s growth, or it could be a stable mode that is excited by smaller-scale processes or extratropical forcing, or a multi-scale mode (or perhaps not even a linear mode at all). As it is still a challenging task to simulate the MJO [26, 22, 49, 7, 41], studies of the nature of the MJO are important for their potential to improve simulations.

This question can be at least partially addressed through the investigation of low-dimensional MJO models. Many such models have been proposed and studied. Some examples of models for the MJO include boundary-layer frictional convergence models [39, 51], moisture mode models [1, 36, 40], and trio-interaction theory [50]. A traditional goal has been to explain the MJO as a linear instability, as in many of the models mentioned above. Other models include the skeleton model [31, 32], which has a neutrally stable MJO in its original formulation, providing an alternative viewpoint.

The question of whether the MJO is a stable or unstable wave cannot be fully studied through just linear eigenmodes, however. Further aspects of the MJO’s behavior need to be assessed. Here we assess not only linear eigenmodes but also variability and nonlinear dynamics, and not only the MJO but also other tropical variability.

For this purpose, a model including both the MJO and CCEWs is needed, and it should have potentially different regimes that may be accessed by changing the background moisture gradient (or other parameters). The two-level convective adjustment model of [42] is well-suited for this purpose as it contains both MJO and CCEW variability. This model was shown to produce a linearly stable MJO that can be activated through stochastic forcing that represents unresolved mesoscale turbulent fluctuations. Since the model of [42] is a linear model, it must be modified to address the MJO’s saturation, and nonlinearities are added here to accomplish

this. Stochastic forcing is omitted here in order to focus on the role these nonlinearities play in saturating the MJO's growth. A 3-D form of the model, which contains a vertically-varying convective adjustment scheme consistent with [42], is presented and used here.

The rest of the paper is organized as follows. The model is presented in Section 2. Linear model solutions are shown in Section 3, and the sensitivity of the MJO's growth rate, frequency, and structure to changes in parameter values are discussed. Nonlinear model solutions are presented in Section 4, and the variability of the MJO and CCEWs in certain parameter regimes is discussed. Additional discussion of the results and other modeling approaches is given in Section 5, and conclusions are given in Section 6.

2 Vertically-varying convective adjustment model

We next present the tropical channel model for MJO and CCEW variability. The methods used to find model solutions are also discussed.

2.1 3-D nonlinear, deterministic model

A 3-D nonlinear, deterministic version of the model of [42] is used. The model consists of the moist hydrostatic Boussinesq equations, with a 2-vertical-mode convective adjustment and moisture diffusion. In dimensional form the equations are

$$\frac{Du}{Dt} - \beta y v + \frac{\partial p}{\partial x} = -\frac{1}{\tau_u} u, \quad (1a)$$

$$\frac{Dv}{Dt} + \beta y u + \frac{\partial p}{\partial y} = -\frac{1}{\tau_u} v, \quad (1b)$$

$$\frac{\partial p}{\partial z} = \frac{g}{\theta_0} \theta, \quad (1c)$$

$$\frac{\partial u}{\partial x} + \frac{\partial v}{\partial y} + \frac{\partial w}{\partial z} = 0, \quad (1d)$$

$$\frac{D\theta}{Dt} + Bw = \frac{L_v}{c_p \tau_{up}} q_{up} + \frac{L_v}{c_p \tau_{mid}} q_{mid} - \frac{1}{\tau_\theta} \theta, \quad (1e)$$

$$\frac{Dq}{Dt} + \frac{\partial q_{bg}}{\partial y} v + \frac{\partial q_{bg}}{\partial z} w = -\frac{1}{\tau_{up}} q_{up} - \frac{1}{\tau_{mid}} q_{mid} + D_h(z) \left(\frac{\partial^2 q}{\partial x^2} + \frac{\partial^2 q}{\partial y^2} \right) + D_v \frac{\partial^2 q}{\partial z^2}, \quad (1f)$$

where $D/Dt = \partial_t + u\partial_x + v\partial_y + w\partial_z$ is the material derivative, $\mathbf{u} = (u, v, w)^T$ is the vector of zonal, meridional, and vertical velocity components of winds, and p is pressure anomalies from a background state. $\theta(x, y, z, t)$ is potential temperature anomalies from a background state $\theta_{BG} = \theta_0 + Bz$. The moisture variable $q(x, y, z, t)$ represents specific humidity anomalies from a background state $q_{BG} = q_0 + q_{bg}(y, z)$, and θ_0 and q_0 are the potential temperature and moisture at $z = 0$, i.e. at the top of the boundary layer. The terms proportional to q_{mid} and q_{up} in (1e) and (1f) are convective adjustment terms which will be discussed in further detail below; these terms serve as the heat source Q in the model.

The only nonlinear terms in the model are nonlinear advection, all contained in the D/Dt terms on the left-hand side of (1). As is common in first efforts with relatively simple models, a resting background state has been used; this simplifies the linear stability analysis and allows for focus on the mechanisms included in the model (e.g., convective adjustment, moisture convergence, eddy diffusion). Other terms in (1) include Rayleigh friction and Newtonian cooling, vertical advection of background potential temperature, and (horizontal and vertical) eddy diffusion of moisture. Forcing terms in [42] have been omitted here resulting in a deterministic model with no Walker circulation; these terms will be added in future work. Parameter definitions and standard values are listed in Table 1.

The convective adjustment scheme used here is a 2-vertical-mode scheme, so that the moisture terms q_{up} and q_{mid} are defined using only the first two baroclinic modes of moisture,

$$q_{up}(x, y, z, t) = Q_{up} \left(\sqrt{2} \sin(\pi z/H) - \frac{\sqrt{2}}{2} \sin(2\pi z/H) \right), \quad (2a)$$

$$q_{mid}(x, y, z, t) = Q_{mid} \sqrt{2} \sin(\pi z/H), \quad (2b)$$

where

$$Q_{up} = q_1 \sqrt{2} \sin \frac{2\pi}{3} + q_2 2\sqrt{2} \sin \frac{4\pi}{3}, \quad (3a)$$

$$Q_{mid} = q_1 \sqrt{2} \sin \frac{\pi}{2}. \quad (3b)$$

The terms $q_1(x, y, t)$ and $q_2(x, y, t)$ represent the first and second baroclinic components of moisture, respectively; i.e.

$$q_1(x, y, t) = \frac{1}{H} \int_0^H q(x, y, z, t) \sqrt{2} \sin(\pi z/H) dz, \quad (4a)$$

$$q_2(x, y, t) = \frac{1}{H} \int_0^H q(x, y, z, t) 2\sqrt{2} \sin(2\pi z/H) dz, \quad (4b)$$

where H is the height of the troposphere. The coefficient 2 in the second baroclinic mode arises from having adopted the convention of defining the j -th baroclinic mode using $j\sqrt{2} \sin(j\pi z/H)$ as in, e.g., [44]. Note that no nonlinear switch is included in the model; an everywhere-precipitating environment is used here. Such a simplification is useful because a nonlinear switch would introduce a mechanism of water loss from the domain, and a compensating source of moisture would need to be parameterized as an additional process with further complication to the model.

This 2-vertical-mode convective adjustment scheme is motivated in part by the facts that the most significant forms of heating in the tropics, i.e. deep, stratiform, and congestus, are well-represented using only the first two baroclinic modes, and that other modeling studies have shown that many tropical atmospheric phenomena are reproduced well by models that have two baroclinic modes of heating [18, 47]. Figure 1 shows the vertical structure of q_{up} and q_{mid} from (2). The profile of q_{mid} resembles that of heating due to deep convection, while the profile of q_{up} is a top-heavy heating profile that can represent stratiform heating. Other motivation for this convective adjustment scheme comes from the observation in [42] that

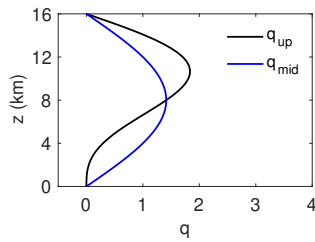


Fig. 1 The vertical structures of the convective adjustment terms q_{up} and q_{mid} with $Q_{up} = Q_{mid} = 1$.

Table 1 Standard parameter values

Parameter	Description	Standard value
H	Height of troposphere	16 km
p_Y	Distance from equator to channel wall	6000 km
β	Variation of Coriolis parameter with latitude	$2.3 \times 10^{-11} \text{ m}^{-1} \text{ s}^{-1}$
g	Acceleration due to gravity	9.8 m s^{-2}
c_p	Specific heat of dry air at constant pressure	$1006 \text{ J kg}^{-1} \text{ K}^{-1}$
L_v	Latent heat of vaporization	$2.5 \times 10^6 \text{ J kg}^{-1}$
B	Background potential temperature vertical gradient	3 K km^{-1}
θ_0	Reference potential temperature	300 K
τ_u	Wind damping timescale	25 d
τ_θ	Potential temperature damping timescale	25 d
τ_{up}	Moisture damping timescale (upper troposphere)	1 d
τ_{low}	Moisture damping timescale (lower troposphere)	2/24 d
B_{vs}	Mean vertical q_{BG} gradient	$-0.00134 \text{ kg kg}^{-1} \text{ km}^{-1}$
a	1 minus pole-to-equator q_{BG} ratio	0.25
\tilde{L}	q_{BG} meridional decay lengthscale	2000 km
$D_{h,up}$	Horizontal q diffusion (upper trop)	$60.8 \text{ km}^2 \text{ s}^{-1}$
$D_{h,mid}$	Horizontal q diffusion (mid trop)	$7.6 \text{ km}^2 \text{ s}^{-1}$
D_v	Vertical q diffusion	$0.0001 \text{ km}^2 \text{ s}^{-1}$

inclusion of two baroclinic modes of moisture was a key ingredient for producing a realistic model MJO, and we note that the linear model of [42], on which the current model is based, can be viewed as a coupling between a traditional convective adjustment model [2, 34] and a model for the background spectrum of tropical convection [14].

Rigid lid boundary conditions are used at the bottom ($z = 0$) and top ($z = H$) of the troposphere. Both moisture and potential temperature anomalies are set to zero at these vertical boundaries. An anelastic version of the model would be interesting to study, and is a topic for future consideration. In the zonal and meridional direction, periodic boundary conditions are used, with the meridional extent of the domain $2p_Y$ (with p_Y the half-width of the channel) taken to be sufficiently large so that effects from the boundaries do not significantly alter the dynamics in the tropics. While the use of periodic boundary conditions in y is unrealistic, it allows for solutions to be found in a straightforward manner, and some testing of the model solver suggests that using a larger meridional domain (channel width) does not significantly affect the results.

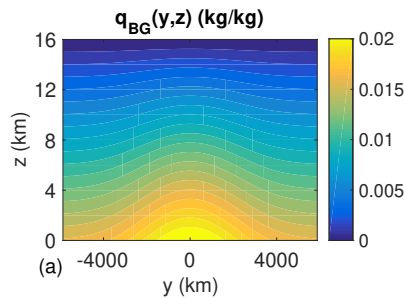


Fig. 2 Background moisture profile $q_{BG}(y, z)$ with $a = 0.25$, $\tilde{L} = 2000$ km.

2.2 Parameter values for ‘standard’ case

Most of the parameter values used here are similar to those used in other recent modeling studies. The convective adjustment times will be set to $\tau_{mid} = 2$ h, which is within the range of values used in other studies [17, 34], and $\tau_{up} = 1$ d, which is similar to the value found in [42] through calibrating the background spectrum of their stochastic model. The u and θ damping rates will be set to $\tau_u = \tau_\theta = 25$ d, which is consistent with findings in [43, 45]. See Table 1 for a list of all parameter values used in Sections 3.1 and 4.1.

The background moisture is shown in Figure 2 and is given by

$$q_{BG}(y, z) = [1 - a(1 - e^{-(y/\tilde{L})^2/2})]q_{BG,EQ}(z) \quad (5)$$

where $q_{BG,EQ}(z) = B_{vs}(z - H)$ is a prescribed vertical profile of background moisture at the equator; the parameters $0 \leq a \leq 1$ and \tilde{L} dictate the background moisture meridional decay away from the equator. The vertical gradient B_{vs} of background moisture is taken to be $-1.34 \text{ g kg}^{-1} \text{ km}^{-1}$, similar to values considered in [10, 11]; this value is significantly larger than those used in [42], and likely more in line with values seen in the tropical atmosphere [13, 35]. The linear profile used here is different than that seen in observations [13], but is consistent with that used in other modeling studies that make use of the Boussinesq approximation; other profiles will also be considered in the parameter sensitivity study.

The diffusion coefficient $D_h(z)$ is defined as $D_h(z) = D_{h,mid} + (D_{h,up}/H)z$, which is essentially a linear interpolation of the mid and lower tropospheric diffusion coefficients from [42]. Here, the values of $D_{h,mid}$ and $D_{h,up}$ are set to be identical to the values used for b_{low} and b_{mid} in [42].

2.3 Implementation of model solvers

The model (1) may be linearized about a resting background state, and solutions of the form $u = \hat{u}_k(y, z)e^{i(kx - \omega t)}$, etc., may be sought for a given zonal wavenumber k . The y and z directions are discretized; the vertical discretization consists of a staggered grid with θ , q and w evaluated at levels $z_j = j\Delta z$ and u , v and p evaluated at levels $z_{j-1/2} = (j - 1/2)\Delta z$, where $\Delta z = H/n_z$ with n_z the number of vertical u levels. Derivatives are calculated spectrally in x and y , and using finite

differences in z . The linearized equations are reformulated using barotropic streamfunction and relative vorticity and the resulting eigenvalue problem for frequency ω is solved. The resolution used for both linear and nonlinear results presented here is $n_x = 48$, $n_y = 48$, and $n_z = 8$ or 10 . Such coarse resolution will not allow for small-scale features to be accurately represented in the results presented here. A more detailed study of the nonlinear dynamics using higher resolution is left to future work, as the focus here is the planetary-scale MJO.

Approximate solutions to the nonlinear model were found using the same staggered grid approach and standard finite difference and spectral methods for evaluating the advection terms. The classical 4th-order Runge-Kutta method is used for time-stepping. For derivatives in x and y , a pseudospectral approach was used, with nonlinearities evaluated in physical space and derivatives evaluated in Fourier space; solutions were dealiased using the standard 2/3 rule.

In order to verify that the solvers work correctly, several straightforward checks were done. In addition to the MJO modes presented here, solutions to the linearized model include standard tropical waves (Kelvin, Rossby, MRG, etc.) and other expected modes (modified by the presence of moisture). The nonlinear solver was checked by finding solutions using one of these linear solutions with small amplitude as an initial condition. After evolving forward in time, the solution's propagation and structure were verified with the linear mode. In a test of simulating a small-amplitude MJO eigenmode in the nonlinear solver, the relative L^2 error after 20 days of simulation was 9.85×10^{-4} . In addition, convergence tests were also done which indicate that the code converges. To test convergence, the standard resolution simulation was supplemented by additional simulations with refined vertical resolution by a factor of 2 and 4; the relative L^2 errors in the standard and two refined simulations after 5 days were 0.007082, 0.001603, and 4.7957×10^{-4} , respectively. Likewise, the standard resolution simulation was supplemented by additional simulations with refined horizontal resolution by a factor of 2 and 4; the relative L^2 errors in the standard and two refined simulations after 5 days were 0.08998, 0.03003, and 1.3054×10^{-4} , respectively.

3 Linear instability of the model MJO

The eigenmodes of the linearized model are now presented. The focus here is on unstable MJO eigenmodes, whose nonlinear evolution will be investigated in subsequent sections.

3.1 Standard case

Figure 3 shows the frequency and growth rate for the standard case MJO, which is the only unstable planetary-scale mode. The MJO is only unstable for zonal wavenumbers $k = 1$ and 2 , with growth rates of roughly 0.02 d^{-1} . We note that there are some unstable modes for zonal wavenumbers $k = 7 - 9$ which appear to be moist Rossby waves; these modes are all westward moving and have growth rates smaller than 0.01 d^{-1} . We focus on the MJO mode for the remainder of this section, returning to CCEWs in Section 4.

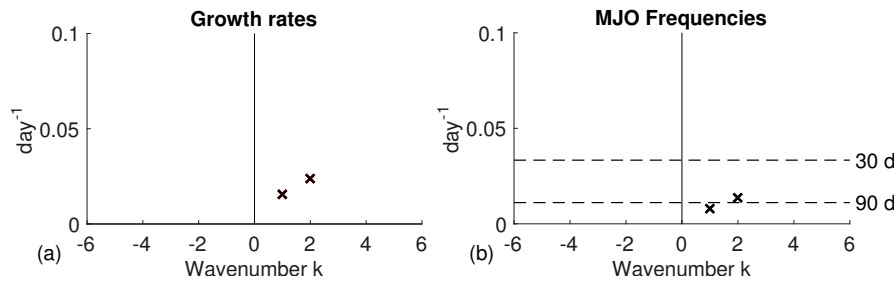


Fig. 3 (a) Growth rates and (b) frequencies of the unstable MJO mode. The $k = 1$ and $k = 2$ MJO modes are the only unstable modes with $|k| \leq 6$; i.e., all positive growth rates for zonal wavenumbers $|k| \leq 6$ are shown.

The frequency of the $k = 2$ MJO mode corresponds to a period and phase speed of 74 days and 3.1 m s^{-1} , respectively; the $k = 1$ MJO mode has period and phase speed of 128 days and 3.6 m s^{-1} , respectively. These frequencies are a little lower than for a typical MJO, though it will be shown in the next section that the nonlinear MJO has a higher phase speed that better matches the observed MJO.

Figure 4 shows the horizontal and vertical structure of the $k = 2$ MJO mode. The horizontal structure in the upper troposphere shows the typical Kelvin-Rossby structure, with a pair of cyclones trailing and a pair of anticyclones leading positive low-level moisture and convergence anomalies. The trailing gyres are slightly closer to the low-level moisture anomalies than the leading gyres, consistent with composites in [20]. The center of the gyres lies somewhere between $15\text{-}20^\circ\text{N}$ and $15\text{-}20^\circ\text{S}$, similar to or slightly closer to the equator than composites [8, 20]. A similar structure emerges for $k = 1$. In the lower troposphere, the Kelvin structure is slightly less prominent, and the gyres have a slightly different tilt than in the upper troposphere (not shown).

The vertical structure shows moisture concentrated in the lower troposphere. A very slight vertical tilt, consistent with composites in observational studies [20], is present in Figure 4(b), though it is barely noticeable. Low-level convergence is also very nearly in phase with low-level moisture anomalies. Potential temperature and wind anomalies are largely first baroclinic, in good agreement with observations. The moisture anomalies are smaller than expected relative to the wind anomalies, a point discussed further in Section 5.

In summary, despite some limitations mentioned above, the model produces a reasonably realistic linearly unstable MJO.

3.2 Parameter sensitivity study

How sensitive are the growth rate and velocity to the parameter values? In particular, how do the values of convective adjustment timescales τ_{up} and τ_{mid} , vertical background moisture gradient B_{vs} , and horizontal diffusion coefficients $D_{h,up}$ and $D_{h,mid}$ impact growth rate and velocity?

Figure 5 shows the growth rate and phase speed of the $k = 1$ MJO mode for various values of each parameter. The standard case MJO, presented in Section 3.1, is denoted by the large red symbols; in each plot, a single parameter is varied while

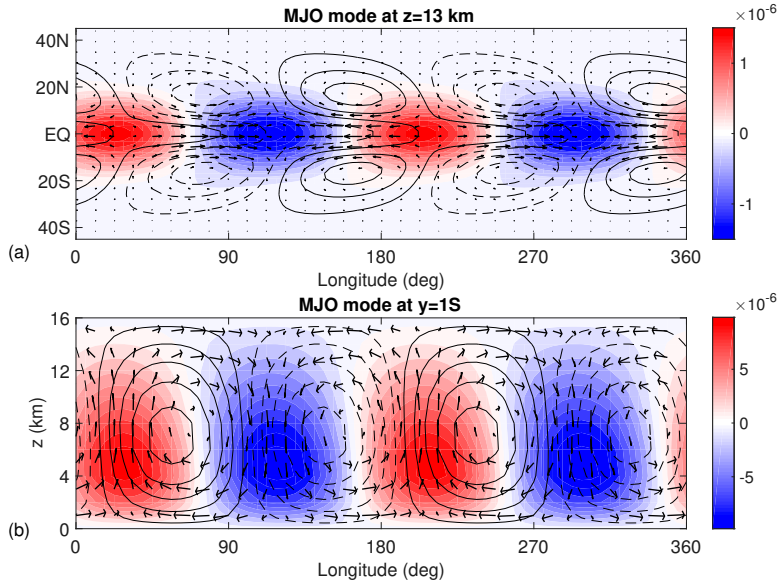


Fig. 4 (a) Horizontal structure of linear MJO mode. Winds are at $z = 13$ km; potential temperature and moisture are at $z = 14$ km. Positive (negative) potential temperature is shown with solid (dashed) contours; contours shown at $1/6$, $1/2$, and $5/6$ the maximum (minimum) potential temperature anomalies. Maximum wind and potential temperature anomalies are 1.2 m s^{-1} and 0.03 K , respectively. Moisture anomalies (kg kg^{-1}) depicted by shading. (b) Vertical structure of linear MJO mode. Zonal winds, potential temperature, and moisture shown at $y = 1\text{S}$. Potential temperature contours shown at $1/10$, $3/10$, $1/2$, $7/10$, and $9/10$ the maximum (minimum) potential temperature anomalies. Maximum wind and potential temperature anomalies are 1.5 m s^{-1} and 0.03 K , respectively. The vertical wind component has been multiplied by a factor of 150 for visual clarity.

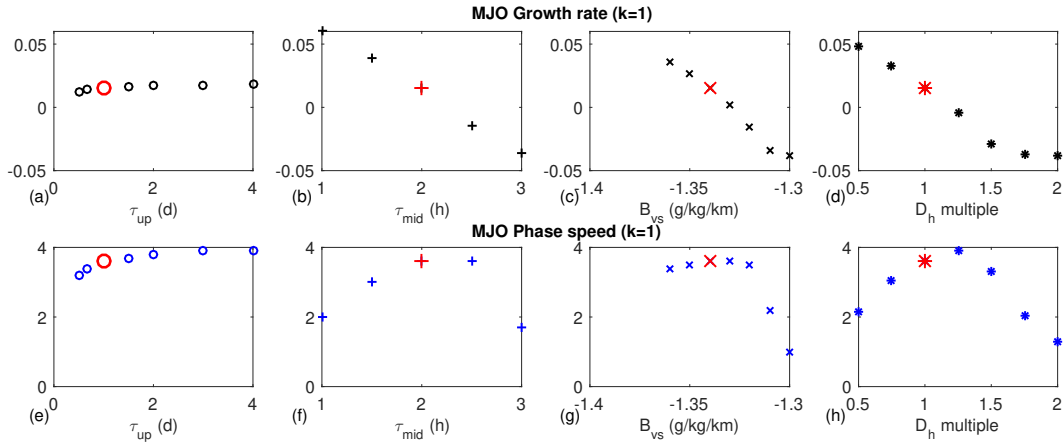


Fig. 5 (a)-(d) MJO $k = 1$ mode growth rate for various values of (a) τ_{up} , (b) τ_{mid} , (c) B_{vs} , and (d) diffusion constant multiple m defined in the text. Large red symbols denote standard values. (e)-(h) MJO $k = 1$ mode phase speed for various values of (e) τ_{up} , (f) τ_{mid} , (g) B_{vs} , and (h) horizontal diffusion constant multiple m .

Table 2 Parameter values for cases shown in Sections 3.2 and 4.2.

Parameter	Description	Case 2	Case 3	Case 4	Case 5	Case 6
B_{vs} (kg kg ⁻¹ km ⁻¹)	Mean vertical q_{BG} gradient	-0.00128	-0.00128	-0.0011	-0.0012	-0.0011
\tilde{s}	controls curvature of $q_{BG}(z)$	12	12	10	12	10
a	1 minus pole-to-equator q_{BG} ratio	0.5	0	0.2	0.2	0.5
\tilde{L}	q_{BG} meridional decay lengthscale	2000	N/A	3000	3000	2000
$D_{h,up}$ (km ² s ⁻¹)	Horizontal q diffusion (upper trop)	121.6	121.6	60.8	60.8	60.8
$D_{h,low}$ (km ² s ⁻¹)	Horizontal q diffusion (lower trop)	15.2	15.2	7.6	7.6	7.6
D_v (km ² s ⁻¹)	Vertical q diffusion	0.0005	0.0005	0.0002	0.0002	0.0002
τ_u, τ_θ (d)	Damping timescales	16	16	16	16	16
τ_{low} (h)	Convective adjustment time	4	4	4	4	4

all other parameters remain at their standard values. Both the growth rate and phase speed are fairly insensitive to changes in τ_{up} , with both the growth rate and phase speed showing a very slight increase as τ_{up} is increased. The results are more sensitive to τ_{mid} and B_{vs} , with the growth rate decreasing with increasing τ_{mid} and increasing B_{vs} . The phase speed increases with increasing τ_{mid} (B_{vs}) until reaching a time of 2 hours (-1.37 g kg⁻¹ km⁻¹); the phase speed then decreases rather sharply as τ_{mid} increases from 3 to 4 hours (and as B_{vs} increases from -1.32 to -1.3 g kg⁻¹).

The diffusion coefficients were varied simultaneously by a multiple, i.e. results will be showed using values $m\tilde{D}_{h,up}$ and $m\tilde{D}_{h,mid}$ for a constant m , where the tilde is used to denote standard case values. Not surprisingly, the growth rates decrease as the diffusion coefficients increase; there is again a non-monotonic response in the phase speed to these changes, with the fastest phase speed of approximately 4 m s⁻¹ occurring for diffusion coefficients that are 1.25 times as large as the standard values.

How sensitive are the growth rate and velocity to the way the convective adjustment terms are defined? For example, what are the effects of using a lower-tropospheric moisture in place of a mid-tropospheric moisture? To briefly examine this, equations (1e) and (1f) will be replaced by

$$\frac{D\theta}{Dt} + Bw = \frac{L_v}{c_p\tau_{up}}q_{up} + \frac{L_v}{c_p\tau_{low}}q_{low} - \frac{1}{\tau_\theta}\theta, \quad (6a)$$

$$\frac{Dq}{Dt} + \frac{\partial q_{bg}}{\partial y}v + \frac{\partial q_{bg}}{\partial z}w = -\frac{1}{\tau_{up}}q_{up} - \frac{1}{\tau_{low}}q_{low} + D_h(z)\left(\frac{\partial^2 q}{\partial x^2} + \frac{\partial^2 q}{\partial y^2}\right) + D_v\frac{\partial^2 q}{\partial z^2}, \quad (6b)$$

respectively, where

$$q_{low}(x, y, z, t) = Q_{low}\left(\sqrt{2}\sin(\pi z/H) + \frac{\sqrt{2}}{2}\sin(2\pi z/H)\right), \quad (7)$$

and where

$$Q_{low} = q_1\sqrt{2}\sin\frac{\pi}{3} + q_22\sqrt{2}\sin\frac{2\pi}{3}. \quad (8)$$

In other words, there are no terms that contain only first baroclinic mode moisture; each term is a combination of the first and second baroclinic modes.

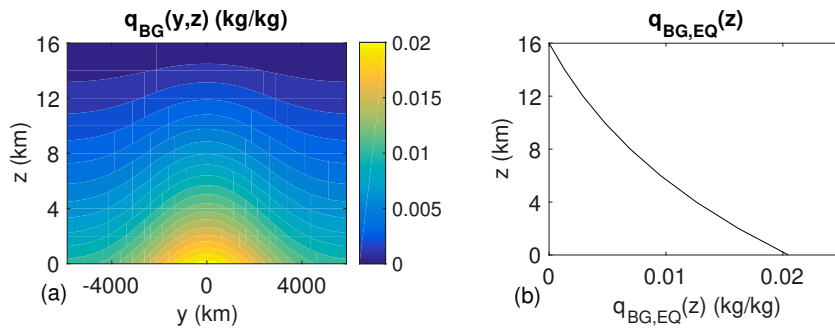


Fig. 6 Case 2 parameter values: (a) Background moisture profile $q_{BG}(y, z)$ and (b) background vertical moisture profile $q_{BG,EQ}(z)$ with $a = 0.25$, $\bar{L} = 2000$ km.

Results are presented using equations (6) with five different sets of parameter values; see Table 2 for parameter values used in each of Cases 2-6. In each case, a slightly stronger damping is used for winds and potential temperature, and the vertical profile of background moisture is defined here to be exponentially decaying as z increases,

$$q_{BG,EQ}(z) = B_{vs} H \frac{e^{-z/\bar{s}} - e^{-H/\bar{s}}}{1 - e^{-H/\bar{s}}} \quad (9)$$

where \bar{s} is a parameter that controls the rate of decay. The background moisture for Case 2 is shown in Figure 6. This curvature allows a reasonable value for B_{vs} to be used and still produce realistic results.

Case 2 creates an MJO not unlike the standard case results in Section 3.1. Case 3 illustrates the effect of a meridionally-constant background moisture profile; Cases 4 and 5 illustrate weaker meridional and vertical gradients of moisture and weaker diffusion than the standard case; Case 6 illustrates weaker diffusion and weaker vertical gradient of moisture.

Figure 7 shows the growth rates and frequencies of the linear modes for Cases 2-6. Cases 2, 3, 4, and 6 all show instability only on planetary scales, and the only unstable mode is an eastward-moving MJO. Each case has a maximum growth rate of roughly 0.05 d^{-1} ; for each case these maximum growth rates occur for wavenumbers $k = 3$ or 4 . The frequencies have a Kelvin-like dispersionless quality over wavenumbers $k = 1$ through 4 , with a drop-off in frequency for higher wavenumbers; most of these frequencies lie within the range $1/30 \text{ d}^{-1}$ to $1/90 \text{ d}^{-1}$, though some are at the low end of this range.

Case 5 also contains a single unstable wave type, namely the MJO; this MJO has higher growth rates than the other cases, with a maximum between 0.25 and 0.3 d^{-1} . The frequencies for $k = 1$ through 4 are all less than $1/90 \text{ d}^{-1}$, and the Kelvin-like nature of the frequencies is more pronounced over all planetary and synoptic scales than in the other cases. Note that Case 5 contains more background moisture than (and identical diffusion coefficients to) Cases 4 and 6, while having weaker diffusion than (and identical moisture to) Cases 2 and 3. The markedly different behavior in the linear solutions shows that the model MJO is strongly excited by this combination of background moisture and diffusion. Case 5 will be explored further in Section 4.

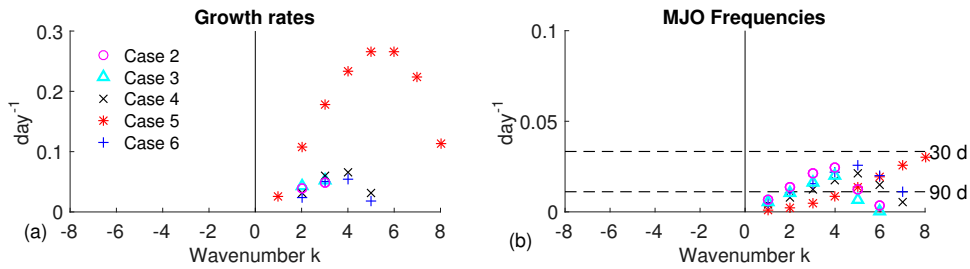


Fig. 7 (a) Growth rates and (b) frequencies of the MJO mode for each case. All positive growth rates are shown; only frequencies associated with MJO modes are shown.

How sensitive is the MJO’s structure to these changes in convective adjustment? Figure 8 depicts the horizontal and vertical structure of the Case 2 $k = 2$ MJO. Similar to the standard case presented above, Case 2 exhibits the mixed Kelvin and Rossby horizontal structure in the winds and potential temperature, moisture anomalies concentrated in the lower troposphere, and low-level convergence roughly in phase with or slightly leading positive moisture anomalies. The vertical structure has some common features with those of the standard case: e.g., slight vertical tilt in moisture, largest moisture anomalies obtained in the lower troposphere. However, the vertical structure is also markedly different, with pronounced second baroclinic potential temperature anomalies, and winds that obtain their strongest values at the bottom of the free troposphere ($z = 0$) and at around $z = 10$ km. This 10 km effective height for the troposphere is also seen in Cases 3-6 (not shown). We note that it is possible that the rigid lid boundary conditions may be partially responsible for the vertical structure, and it would be informative to pursue an anelastic model. However, the success of the model at producing a realistic MJO using mid-tropospheric convective adjustment terms (Sections 2, 3, and 4) suggests that the different convective adjustment scheme implementation is responsible for this change. These results suggest that the MJO’s stability likely depends on background moisture gradients and other parameters.

4 Nonlinear evolution of the model MJO

Solutions to the full nonlinear model (1) are now presented and discussed. Recall that a main motivating question of the present paper is to investigate whether the MJO is a stable or unstable wave. To probe this question in the unstable regime, we now assess not only the model’s nonlinear MJO evolution but also other tropical variability such as CCEWs.

4.1 Standard case

Is the nonlinear model able to slow the growth of this linearly unstable MJO and produce a nonlinear MJO with reasonable amplitude, structure, speed, and dynamics? To answer this, an initial condition consisting of a superposition of a $k = 1$ and 2 linear MJO mode is used in the nonlinear model solver; other modes are omitted in order to focus on the evolution of the MJO. The nonlinear code is

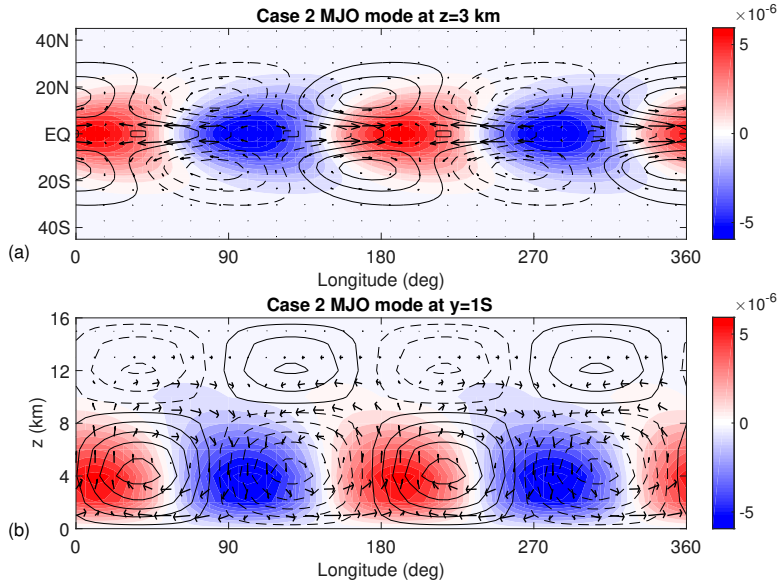


Fig. 8 (a) Horizontal structure of linear MJO mode. Winds are at $z = 3$ km; potential temperature and moisture are at $z = 4$ km. Positive (negative) potential temperature is shown with solid (dashed) contours; contours shown at $1/6$, $1/2$, and $5/6$ the maximum (minimum) potential temperature anomalies. Maximum wind and potential temperature anomalies are 1.2 m s^{-1} and 0.17 K , respectively. Moisture anomalies (kg kg^{-1}) depicted by shading. (b) Vertical structure of linear MJO mode. Zonal winds, potential temperature, and moisture shown at $y = 1\text{S}$. Potential temperature contours shown at $1/10$, $3/10$, $1/2$, $7/10$, and $9/10$ the maximum (minimum) potential temperature anomalies. Maximum wind and potential temperature anomalies are 2.0 m s^{-1} and 0.09 K , respectively. The vertical wind component has been multiplied by a factor of 150.

run for 400 days, and the amplitude, speed, and structure of the resulting wave and its evolution are studied.

Figure 9 shows snapshots at 40-day intervals of the vertical structure of the evolving MJO at the equator and its horizontal structure in the upper troposphere. During the first 60 days, the wave propagates with growing amplitude at the rate predicted by linear theory. Between days 60 and 140, the effects of the nonlinearities become apparent. The zonal extent of the region of positive moisture and convergence anomalies shrinks slightly, similar to other nonlinear models of the MJO [3, 32, 48, 52]. The positive moisture anomalies retain a slight vertical tilt. While the model has selected a wavenumber-1 MJO, there are smaller scale features that are evident once the solution has grown sufficiently outside of the linear regime, and the nonlinear terms transfer energy to smaller scales. The model's selection of a wavenumber-1 MJO is interesting given the linear growth rate is highest for $k = 2$; this selection may depend on initial conditions and is not taken as a fundamental feature of the model. The horizontal structure shows anticyclones that become elongated and weaker. Both the Kelvin and Rossby structures remain apparent throughout the evolution.

By day 160 the MJO has settled into a quasi-steady state, and a primary question is whether the wave has reasonable amplitude. In Figure 9(h), the largest

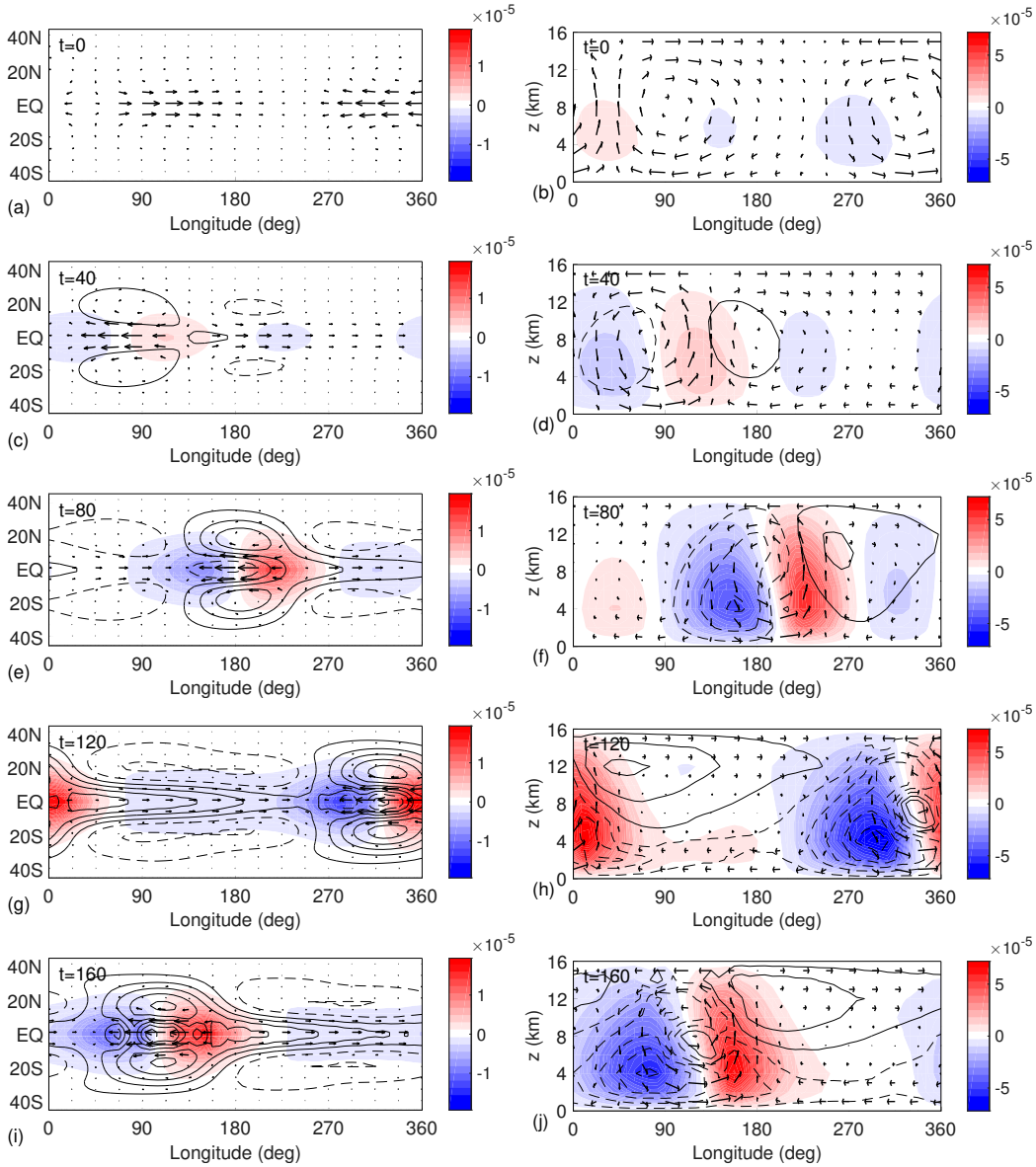


Fig. 9 (a,c,e,g,i) Horizontal structure of nonlinear MJO solution at $t = 0, 40, 80, 120,$ and 160 days. Winds are at $z = 13$ km; potential temperature and moisture are at $z = 14$ km. Positive (negative) potential temperature is shown with solid (dashed) contours; contours shown at $1/10, 3/10, 1/2, 7/10,$ and $9/10$ the maximum (minimum) potential temperature anomalies of 0.33 K. Maximum wind anomalies are (a) 1.2 m s $^{-1}$, (c) 2.9 m s $^{-1}$, (e) 7.4 m s $^{-1}$, (g) 11.3 m s $^{-1}$, (i) 10.8 m s $^{-1}$. Moisture anomalies (kg kg^{-1}) depicted by shading. (b,d,f,h,j) Vertical structure of nonlinear MJO solution. Zonal winds, potential temperature, and moisture shown at $y=1\text{S}$. Potential temperature contours shown at $1/10, 3/10, 1/2, 7/10,$ and $9/10$ the maximum (minimum) potential temperature anomalies of 0.63 K. Maximum wind anomalies are (b) 1.5 m s $^{-1}$, (d) 4.1 m s $^{-1}$, (f) 13.9 m s $^{-1}$, (h) 21.1 m s $^{-1}$, (j) 18.0 m s $^{-1}$. The vertical wind component has been multiplied by a factor of 150 .

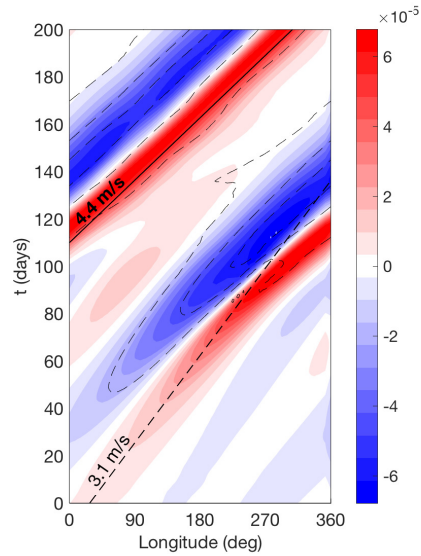


Fig. 10 Hovmöller diagram of nonlinear MJO solution at $z = 4$ km at the equator for the first 200 days of the simulation. Negative potential temperature anomalies are shown with dashed gray contours; contours shown at $1/6$, $1/2$, and $5/6$ the maximum potential temperature anomaly of 0.65 K. Moisture anomalies (kg kg^{-1}) depicted with shading.

wind anomalies are approximately 21 m s^{-1} , which is larger than values seen in composites like in [20] by as much as a factor of 4-5, depending on location and pressure level; such differences could be due to many possible factors that differentiate this model solution from nature, such as Boussinesq dynamical core, lack of warm pool, or lack of other physical mechanisms that may slightly alter the basic model MJO seen here; such differences could also be due to a mismatch in comparing the model's individual MJO event versus a statistical composite, since some individual events will have stronger amplitude than a composite structure. The moisture anomalies remain smaller than those seen in observations, with lower troposphere anomalies up to 0.08 g kg^{-1} . Considering the relative simplicity of the model, relative to other recently developed models, and the fact that the present model has a simplified convective adjustment scheme that does not even include a nonlinear switch, these values seem somewhat reasonable. The potential temperature anomalies are again largely first baroclinic with some vertical tilt. As with the linear solutions, moisture anomalies are more prominent in the lower troposphere.

Figure 10 shows the unfiltered evolution of the wave's potential temperature and moisture anomalies at the equator and in the lower troposphere. Between day 60 and 120, as the nonlinear effects are becoming more apparent, the MJO speeds up from a linear speed of roughly 3.1 m s^{-1} to a speed of approximately 4.4 m s^{-1} , in very good agreement with observed MJOs [20, 54]. This planetary signal is evident in the upper troposphere as well (not shown).

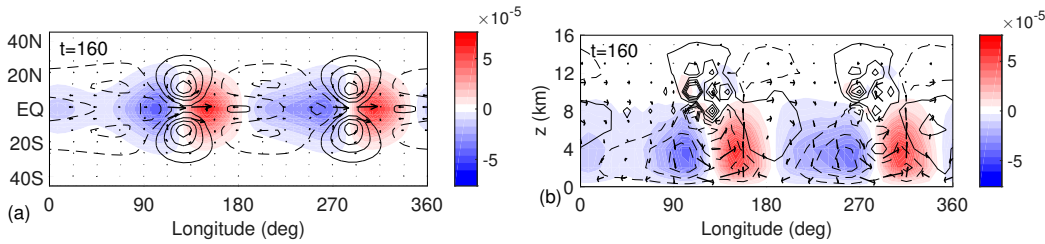


Fig. 11 (a) Horizontal structure of nonlinear Case 2 MJO solution at $t = 160$ days. Winds are at $z = 3$ km; potential temperature and moisture are at $z = 4$ km. Positive (negative) potential temperature is shown with solid (dashed) contours; contours shown at $1/10$, $3/10$, $1/2$, $7/10$, and $9/10$ the maximum (minimum) potential temperature anomalies. Maximum wind and potential temperature anomalies are 16.7 m s^{-1} and 1.9 K , respectively. Moisture anomalies (kg kg^{-1}) depicted by shading. (b) Vertical structure of nonlinear Case 2 MJO solution. Zonal winds, potential temperature, and moisture shown at $y=1\text{S}$. Potential temperature contours shown at $1/10$, $3/10$, $1/2$, $7/10$, and $9/10$ the maximum (minimum) potential temperature anomalies. Maximum wind and potential temperature anomalies are 20.4 m s^{-1} and 2.1 K , respectively. The vertical wind component has been multiplied by a factor of 150.

4.2 Parameter sensitivity study

How robust are the nonlinear MJO's structure and speed to changes in parameter values? To briefly explore this, Figure 11 shows a snapshot at day 160 of the nonlinear evolution of the Case 2 MJO. The initial conditions consisted of a superposition of several zonal wavenumbers ($k = 1 - 3$) of the MJO. Many features of this MJO are reminiscent of the standard case, but noticeable differences exist. Interestingly, there is a narrower zonal extent of moisture and convergence anomalies and cyclones and a wider zonal extent of the anticyclones. The wind and moisture amplitudes obtained are similar to those of the standard case, while the potential temperature anomalies are stronger in Case 2. Finally, the vertical structure is similar to the linear solution in Figure 8 with wind anomalies tapering to zero at the tropopause, likely due to the implementation of the convective adjustment scheme in Case 2.

4.3 CCEW variability

Is the large-scale linear instability of the MJO, by itself, enough to generate variability of CCEWs? Can a model without tropical-extratropical interactions, stochastic forcing representing mesoscale processes, and other mechanisms omitted here produce such variability? In short, it depends on the parameter regime considered. We present results of one parameter regime that does produce such variability by exploring Case 5 further.

Solutions are again found to the nonlinear model with lower tropospheric convective adjustment using an initial condition consisting of a superposition of multiple wavenumbers of both symmetric and anti-symmetric modes. Specifically, zonal wavenumbers $k = 1$ through 3 of the four most unstable or least stable modes were used to construct the initial condition. The model was run for 500 days; it took roughly 70 days for the model to settle into a statistical steady state. Different initial conditions were not extensively tested, but limited testing indicated that all

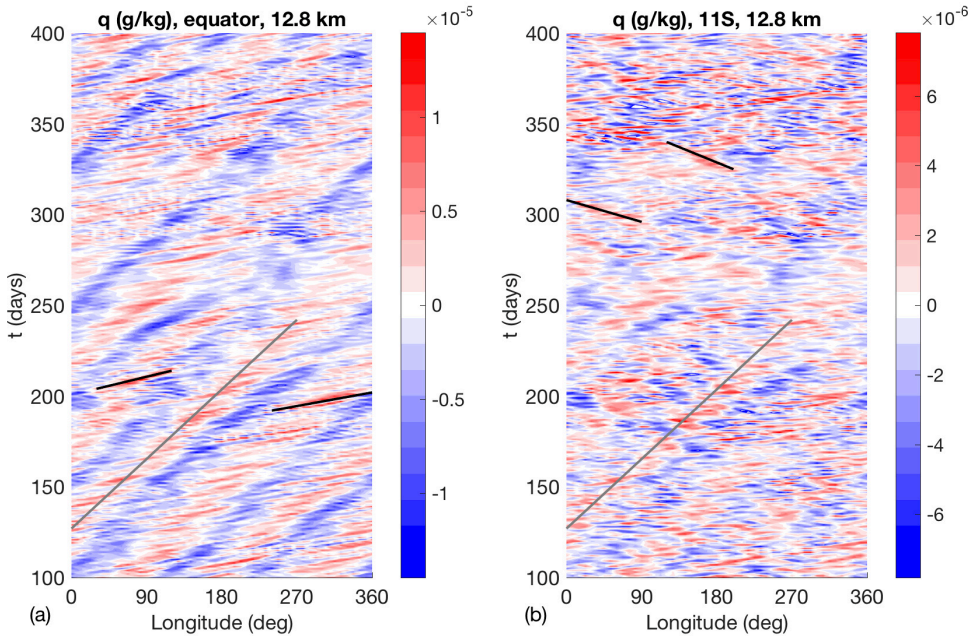


Fig. 12 Hovmöller diagrams of solution from Figure 13. (a) Equator, 12 km; (b) 11S, 12 km. Grey lines denote MJO events; black lines denote convectively coupled (a) Kelvin waves, (b) Rossby waves.

other initial conditions that contained both symmetric and anti-symmetric modes produced similar results.

While the only linearly unstable wave is the MJO, the presence of several wave types in the initial condition results in richer dynamics that include both an MJO and CCEWs. Figure 12 shows Hovmöller diagrams of moisture at 12.8 km and at two latitudes. At the equator, the dominant signal is that of the MJO, which largely has a wavenumber-3 structure, though incidents of termination of positive moisture anomalies associated with the MJO can be seen at around $x = 180$ near day 250, and there appear to be instances of two distinct MJO bands forming from one band at, e.g., around $x = 90$ near days 300 through 320. There is also clear evidence of convectively coupled Kelvin waves throughout the simulation, some of which occur within the MJO envelope. At 11S, several convectively coupled equatorial Rossby wave events can be seen, including, e.g., at $x = 45$ around day 300, and again at $x = 150$ around day 335. Higher frequency wave activity is also clearly present during the simulation, and a number of such events are particularly clear during days 340-370. Similar results can be seen in the lower troposphere, where the prominence of the MJO signal makes it somewhat easier to see incidents of MJO initiation and termination, but slightly more difficult to discern the variety of CCEWs present.

How strong do these waves appear in the wavenumber-frequency power spectrum? The power spectra of the moisture anomalies shown in Figure 12 are constructed using overlapping 128-day segments of data, with each successive segment beginning 38 days after the previous one, in a manner similar to, e.g., [53]. These

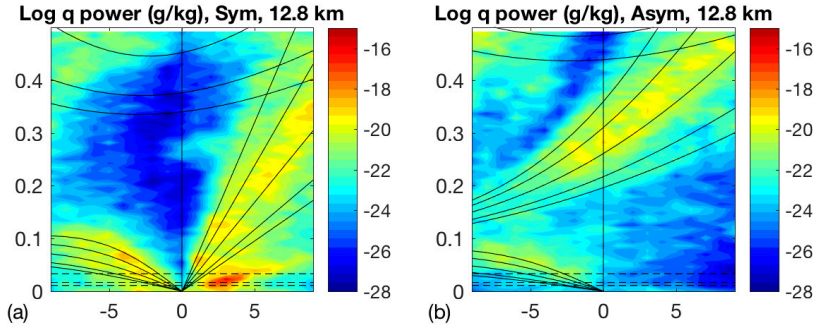


Fig. 13 Case 5 zonal wavenumber-frequency power spectra of the (a) symmetric component and (b) anti-symmetric component of moisture at $z = 12.8$ km.

segments began after the simulation had reached a statistical steady state. Time series of the symmetric and anti-symmetric components of moisture were calculated in the standard way using data from $-p_Y/2$ to $p_Y/2$, where the channel width is $2p_Y$; i.e. the meridional domain is $-p_Y \leq y \leq p_Y$. The first and last ten percent of each time series was tapered using a cosine function, and a discrete Fourier transform was taken in both space and time of the tapered time series.

Figure 13 shows the log of the square of the amplitude of the resulting Fourier coefficients in the upper troposphere. The largest power peak in all variables occurs at $k = 3$ near an eastward frequency of $1/60 \text{ d}^{-1}$, consistent with Figure 12. This peak is part of a band of frequencies that lie in the MJO range but exhibit a tilt that suggests a lack of dispersion, similar to the linear results, whereas observational MJO power does not typically display such a tilt. Note that in the MJO frequency range, eastward symmetric power is much larger than westward power.

Other signals are also clearly discernible, including evidence of convectively coupled Kelvin, Rossby, and MRG-like wave propagation. The power spectra shown are total power spectra, and it is a bit surprising that the spectra are not redder; the lower troposphere, however, shows a redder spectra with peaks that are more difficult to discern (not shown). The absence of an accurate background spectrum suggests that the model instability cannot fill in the background at this resolution and that some combination of tropical-extratropical interactions, higher resolution, and other processes modeled in [42] with stochasticity, plays a critical role in creating the full picture of tropical variability.

Do these results persist for other parameter combinations? In many of the cases presented earlier, the only linearly unstable or barely stable mode is the MJO; as a result, nonlinear simulations using these parameter values produce an MJO and little else, similar to Figures 9 and 11. This suggests that a realistic power spectrum, in the current modeling framework, requires either (i) extratropical forcing or stochastic forcing as in [42] or (ii) deterministic instability arising in a different parameter regime than those of most cases considered here, and an investigation of the nonlinear stability of the model MJO in each parameter regime is left for future work. The appearance of clear CCEW and MJO signals, however, provides reassurance that the model is able to recreate these important features of the model in [42] even without stochastic forcing here, and the richness of the

dynamics indicate that the model may prove useful for future investigations of the nonlinear stability and dynamics of the MJO and CCEWs.

5 Discussion

In this section, we discuss some additional model features or model variations that either yielded unpromising results in other tests or would be interesting to test in the future.

An additional nonlinearity that could be included in future work is a nonlinear switch for precipitation. Inclusion of a nonlinear switch would allow the creation of both non-cloudy regions and convectively active regions, and it should allow for moisture anomalies (below saturation) to persist on longer timescales, resulting in an MJO with larger moisture anomalies. The nonlinear switch was left out of the present model for simplicity, as one would need to also introduce an accompanying moisture source into the model, which comes at the cost of greater model complexity. It would be interesting in the future to include these and other additional features.

Other models and convective parameterizations were tested during this study. A planetary-scale, hydrostatic, Boussinesq version of the Fast Autoconversion and Rain Evaporation (FARE) model [11] was implemented. Some promising results were identified, though the structures that arose from the model were not in such good agreement with observations as those discussed here, and further study of the solutions is left to future work. In addition, a convective parameterization using full vertical resolution, rather than a 2-mode truncation, was also tried; e.g., (1e) was replaced with

$$\frac{D\theta}{Dt} + Bw = \frac{L_v}{c_p\tau(z)}q - \frac{1}{\tau_\theta}\theta, \quad (10)$$

with a similar change to (1f). The vertical structures associated with these modes were complicated by the detailed resolution, and a simpler scheme that emphasized top-heavy and bottom-heavy heating profiles was chosen instead.

6 Conclusions

In the present paper, we investigated instabilities in tropical fluid dynamics, which involves interactions of moisture and dispersive equatorial waves. One of the motivating questions was to investigate whether the MJO is a stable or unstable wave. To probe this question, we considered a tropical channel model that is 3D and nonlinear, with an unstable MJO. The model's dynamics was assessed in terms of not only linear eigenmodes but also nonlinear variability, and not only the MJO but also other aspects of tropical variability such as CCEWs.

In summary, the model is able to produce a linearly unstable MJO with reasonable growth rate, phase speed, and structure. The nonlinearities in the model cause the MJO to also saturate with reasonable amplitude, speed, and structure. In some parameter regimes, CCEW variability is also generated by this unstable MJO. The unstable MJOs produced here, combined with the forced stable ones presented in the linear model [42] show that the model is compatible with either

viewpoint of MJO stability (i.e., that the MJO is a forced stable mode vs. an unstable mode), and suggest that the MJO's stability likely depends on background moisture gradients and other parameters.

The model uses a 2-baroclinic-mode convective adjustment scheme to allow for different response time scales of upper- versus mid-tropospheric moisture. The slower response in the mid-upper troposphere was found to be a key ingredient in producing tropical variability in both the original model and the nonlinear version studied here, and this slower response is in agreement with other studies of convective adjustment [37] and is consistent with the time scale associated with the background spectrum of tropical convection [14, 46, 53].

The 2-vertical-mode convective adjustment scheme is a simple convective parameterization that was effective in this model at producing a realistic MJO. The model's success suggests that it can provide an effective foundation for future studies. For example, it would be interesting and potentially useful to introduce this convective parameterization into a GCM with the goal of reproducing the successful MJO found here. Finally, it was noted that several physical mechanisms are not present in the model, including forcing (no warm pool or Walker circulation), stochasticity, vertical moisture flux, or nonlinear switches; several of these mechanisms will be explored in future work.

Another question is: What is the source of tropical variability (on synoptic/planetary scales)? Many sources are possible, such as instabilities of the MJO or CCEWs (which could further transfer energy from MJO instability to stable CCEWs, as in the present paper), tropical sources such as stochastic mesoscale fluctuations, or extratropical influence. This is another interesting topic for future research. Here we were able to explore one possibility: How much tropical variability can be generated by MJO instability alone (without additional sources)? Certainly the MJO can be generated from an MJO instability, but the background spectrum was lacking in these cases; and while CCEW variability was generated, it was only in a subset of cases where the MJO instability spans several wavenumbers.

Acknowledgements The research of S.H. is partially supported by the National Science Foundation under Grant No. DMS-1815061.

References

1. Adames, Á F. and Kim, D. (2016). The MJO as a dispersive, convectively coupled moisture wave: Theory and observations. *J. Atmos. Sci.* **73**, 913–941.
2. Betts, A. K. and Miller, M. J. (1986). A new convective adjustment scheme. Part II: Single column tests using GATE wave, BOMEX, ATEX, and arctic air mass data sets. *Quart. J. Roy. Meteor. Soc.* **112**, 693–709.
3. Chen, S. and Stechmann, S. N. (2016). Nonlinear traveling waves for the skeleton of the Madden-Julian oscillation. *Comm. Math. Sci.* **14**, 571–592.
4. Dias, J., Leroux, S., Tulich, S. N., and Kiladis, G. N. (2013). How systematic is organized tropical convection within the MJO? *Geophys. Res. Lett.* **40**, 1420–1425.
5. Dias, J., Sakaeda, N., Kiladis, G. N., and Kikuchi, K. (2017). Influences of the MJO on the space-time organization of tropical convection. *J. Geophys. Res. Atmos.* **122**, 8012–8032.
6. Gill, A. E. (1982). *Atmosphere–Ocean Dynamics*. 662 pp. Academic Press. San Diego, CA.
7. Gottschalck, J., Wheeler, M., Weickmann, K., Vitart, F., Savage, N., Lin, H., Hendon, H., Waliser, D., Sperber, K., Nakagawa, M., Prestrelo, C., Flatau, M., and Higgins, W. (2010). A framework for assessing operational Madden-Julian oscillation forecasts. *Bull. Amer. Meteor. Soc.* **91**, 1247–1258.

8. Hendon, H. H. and Salby, M. L. (1994). The life cycle of the Madden-Julian oscillation. *J. Atmos. Sci.* **51**, 2225–2237.
9. Hendon, H. H., Wheeler, M., and Zhang, C. (2007). Seasonal dependence of the MJO–ENSO relationship. *J. Clim.* **20**, 531–543.
10. Hernandez-Duenas, G., Majda, A. J., Smith, L. M., and Stechmann, S. N. (2013). Minimal models for precipitating turbulent convection. *J. Fluid Mech.* **717**, 576–611.
11. Hernandez-Duenas, G., Smith, L. M., and Stechmann, S. N. (2015). Stability and instability criteria for idealized precipitating hydrodynamics. *J. Atmos. Sci.* **72**, 2379–2393.
12. Hittmeir, S. and Klein, R. (2018). Asymptotics for moist deep convection I: refined scalings and self-sustaining updrafts. *Theor. Comput. Fluid Dyn.* **32**, 137–164.
13. Holloway, C. E. and Neelin, J. D. (2009). Moisture vertical structure, column water vapor, and tropical deep convection. *J. Atmos. Sci.* **66**, 1665–1683.
14. Hottovy, S. and Stechmann, S. N. (2015). A spatiotemporal stochastic model for tropical precipitation and water vapor dynamics. *J. Atmos. Sci.* **72**, 4721–4738.
15. Jones, C. (2000). Occurrence of extreme precipitation events in California and relationships with the Madden-Julian oscillation. *J. Climate* **13**, 3576–3587.
16. Jones, C., Waliser, D. E., Lau, K. M., and Stern, W. (2004). The Madden-Julian oscillation and its impact on Northern Hemisphere weather predictability. *Mon. Wea. Rev.* **132**, 1462–1471.
17. Khouider, B. and Majda, A. J. (2006). A simple multicloud parameterization for convectively coupled tropical waves. Part I: Linear analysis. *J. Atmos. Sci.* **63**, 1308–1323.
18. Khouider, B., St-Cyr, A., Majda, A. J., and Tribbia, J. (2011). The MJO and convectively coupled waves in a coarse-resolution GCM with a simple multi-cloud parametrization. *J. Atmos. Sci.* **68**, 240–264.
19. Kikuchi, K., Kiladis, G. N., Dias, J., and Nasuno, T. (2017). Convectively coupled equatorial waves within the MJO during CINDY/DYNAMO: slow Kelvin waves as building blocks. *Clim. Dyn.* DOI 10.1007/s00382-017-3869-5.
20. Kiladis, G. N., Straub, K. H., and Haertel, P. T. (2005). Zonal and vertical structure of the Madden-Julian oscillation. *J. Atmos. Sci.* **62**, 2790–2809.
21. Kiladis, G. N., Wheeler, M. C., Haertel, P. T., Straub, K. H., and Roundy, P. E. (2009). Convectively coupled equatorial waves. *Rev. Geophys.* **47**, RG2003.
22. Kim, D., Sperber, K., Stern, W., Waliser, D., Kang, I.-S., Maloney, E., Wang, W., Weickmann, K., Benedict, J., Khairoutdinov, M., Lee, M.-I., Neale, R., Suarez, M., Thayer-Calder, K., and Zhang, G. (2009). Application of MJO simulation diagnostics to climate models. *J. Climate* **22**, 6413–6436.
23. Klein, R. and Majda, A. J. (2006). Systematic multiscale models for deep convection on mesoscales. *Theor. Comput. Fluid Dyn.* **20**, 525–551.
24. Lau, W. K. M. and Waliser, D. E. (2012). *Intraseasonal Variability in the Atmosphere–Ocean Climate System*, Springer, Berlin.
25. Liebmann, B., Hendon, H. H., and Glick, J. D. (1994). The relationship between tropical cyclones of the Western Pacific and Indian oceans and the Madden-Julian oscillation. *J. Meteor. Soc. Japan*, **72**, 10.2151/jmsj1965.72.3.401.
26. Lin, J.-L., Kiladis, G. N., Mapes, B. E., Weickmann, K. M., Sperber, K. R., Lin, W., Wheeler, M. C., Schubert, S. D., Del Genio, A., Donner, L. J., Emori, S., Gueremy, J.-F., Hourdin, F., Rasch, P. J., Roeckner, E., and Scinocca, J. F. (2006). Tropical intraseasonal variability in 14 IPCC AR4 climate models. Part I: convective signals. *J. Climate* **19**, 2665–2690.
27. Madden, R. A. and Julian, P. R. (1971). Detection of a 40–50 day oscillation in the zonal wind in the tropical Pacific. *J. Atmos. Sci.* **28**, 702–708.
28. Madden, R. A. and Julian, P. R. (1972). Description of global-scale circulation cells in the tropics with a 40–50 day period. *J. Atmos. Sci.* **29**, 1109–1123.
29. Madden, R. A. and Julian, P. R. (1994). Observations of the 40–50-day tropical oscillation - a review. *Mon. Wea. Rev.* **122**, 814–837.
30. Majda, A. J. (2003). *Introduction to PDEs and Waves for the Atmosphere and Ocean*. Courant Lecture Notes in Mathematics (American Mathematical Society, Providence, RI) Vol 9.
31. Majda, A. J. and Stechmann, S. N. (2009). The skeleton of tropical intraseasonal oscillations. *Proc. Natl. Acad. Sci.* **106**, 8417–8422.
32. Majda, A. J. and Stechmann, S. N. (2011). Nonlinear dynamics and regional variations in the MJO skeleton. *J. Atmos. Sci.* **68**, 3053–3071.

33. Maloney, E. D. and Hartmann, D. L. (2000). Modulation of the Eastern North Pacific hurricanes by the Madden-Julian oscillation. *J. Climate* **13**, 1451–1460.
34. Neelin, J. D. and Yu, J.-Y. (1994). Modes of tropical variability under convective adjustment and the Madden-Julian oscillation. Part 1: Analytical theory. *J. Atmos. Sci.* **51**, 1876–1894.
35. Peixoto, J. P. and Oort, A. H. (1992). *Physics of Climate*. (American Institute of Physics, New York, NY)
36. Raymond, D. J. and Fuchs, Ž. (2009). Moisture modes and the Madden-Julian oscillation. *J. Climate* **22**, 3031–3046.
37. Raymond, D. J. and Herman, M. J. (2011). Convective quasi-equilibrium reconsidered. *J. Adv. Model. Earth Syst.* **3**, Art. 2011MS000079.
38. Rui, H. and Wang, B. (1990). Development characteristics and dynamic structure of tropical intraseasonal convection anomalies. *J. Atmos. Sci.* **47**, 357–379.
39. Salby, M. L., Garcia, R. R. and Hendon, H. H. (1994). Planetary-scale circulations in the presence of climatological and wave-induced heating. *J. Atmos. Sci.* **51**, 2344–2367.
40. Sobel, A. and Maloney, E. (2013). Moisture modes and the eastward propagation of the MJO. *J. Atmos. Sci.* **70**, 187–192.
41. Sperber, K. R. and Kim, D. (2012). Simplified metrics for the identification of the Madden-Julian oscillation in models. *Atmos. Sci. Lett.* **13**, 187–193.
42. Stechmann, S. N. and Hottovy, S. (2017). Unified spectrum of tropical rainfall and waves in a simple stochastic model. *Geophys. Res. Lett.* **44**, 10,713–10,724.
43. Stechmann, S. N. and Majda, A. J. (2015). Identifying the skeleton of the Madden-Julian oscillation in observational data. *Mon. Wea. Rev.* **143**, 395–416.
44. Stechmann, S. N., Majda, A. J., and Khouider, B. (2008). Nonlinear dynamics of hydrostatic internal gravity waves. *Theor. Comp. Fluid Dyn.* **22**, 407–432.
45. Stechmann, S. N. and Ogrosky, H. R. (2014). The Walker circulation, diabatic heating, and outgoing longwave radiation. *Geophys. Res. Lett.* **41**, 9097–9105.
46. Takayabu, Y. N. (1994). Large scale cloud disturbances associated with equatorial waves. Part I: Spectral features of the cloud disturbances. *J. Meteor. Soc. Japan* **72**, 433–449.
47. Thual, S. and Majda, A. J. (2015). A Suite of Skeleton Models for the MJO with Refined Vertical Structure. *Math. of Cli. and Weather For.* **1**, 2353–6438.
48. Thual, S., Majda, A. J., and Stechmann, S. N. (2014). A stochastic skeleton model for the MJO. *J. Atmos. Sci.* **71**, 697–715.
49. Waliser, D., Sperber, K., Hendon, H., Kim, D., Maloney, E., Wheeler, M., Weickmann, K., Zhang, C., Donner, L., Gottschalck, J., Higgins, W., Kang, I.-S., Legler, D., Moncrieff, M., Schubert, S., Stern, W., Vitart, F., Wang, B., Wang, W. and Woolnough, S. (2009). MJO Simulation Diagnostics. *J. Climate* **22**, 3006–3030.
50. Wang, B., Liu, F., and Chen, G. (2016). A trio-interaction theory for Madden-Julian oscillation. *G. Geosci. Lett.* **3**, 34. DOI 10.1186/s40562-016-0066-z
51. Wang, B. and Rui, H. (1990). Dynamics of the coupled moist Kelvin–Rossby wave on an equatorial beta-plane. *J. Atmos. Sci.* **47**, 397–413.
52. Wei, Y., Liu, F., Mu, M. and Ren, H.-L. (2017). Planetary scale selection of the Madden–Julian Oscillation in an air-sea coupled dynamic moisture model. *Clim. Dyn.* <https://doi.org/10.1007/s00382-017-3816-5>.
53. Wheeler, M. and Kiladis, G. N. (1999). Convectively coupled equatorial waves: Analysis of clouds and temperature in the wavenumber-frequency domain. *J. Atmos. Sci.* **56**, 374–399.
54. Zhang, C. (2005). Madden-Julian oscillation. *Rev. Geophys.* **43**, RG2003.
55. Zhang, C., Gottschalck, J., Maloney, E. D., Moncrieff, M. W., Vitart, F., Waliser, D. E., Wang, B. and Wheeler, M. C. (2013). Cracking the MJO nut. *Geophys. Res. Lett.* **40**, 1223–1230.